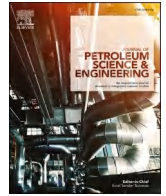




Contents lists available at ScienceDirect

Journal of Petroleum Science and Engineering

journal homepage: <http://www.elsevier.com/locate/petrol>

XFEM-based numerical modeling of well performance considering proppant transport, embedment, crushing and rock creep in shale gas reservoirs

Fang Shi^{a,b}^a Faculty of Mechanical & Material Engineering, Huaiyin Institute of Technology, Huai'an, Jiangsu, 223003, China^b CAS Key Laboratory of Mechanical Behavior and Design of Materials, Department of Modern Mechanics, University of Science and Technology of China, Hefei, Anhui, 230027, China

ARTICLE INFO

Keywords:

Hydraulic fracturing
Gas production
Proppant crushing
Shale creep
XFEM

ABSTRACT

Predicting the production rate and estimating the ultimate recovery are of great significance for the optimization of shale gas development. One possible reason for production decline is the width reduction of propped fractures caused by proppant deformation, embedment, crushing, and viscoelasticity of the reservoir. In order to obtain more in-depth knowledge of how these factors influence the gas production, a novel approach is proposed to simulate the processes of both hydraulic fracturing and gas production using the extended finite element method (XFEM). On the one hand, a numerical model which involves the coupled processes of deformation of the porous rock medium, fluid flow and leak-off, crack propagation, and proppant transport is proposed to obtain the proppant distribution for the hydraulic fracturing simulation. On the other hand, a coupled rock deformation and two-phase flow model considering stress-dependent fracture conductivity, crushing of proppant grains, creep of surrounding rock, gas diffusion and desorption, and influence of natural fractures is developed for the flowback and gas production simulation. The fracture closure during the shut-in and flowback process of fracturing fluid is considered. In addition, the size effects of proppant grains are investigated by using Weibull theory. After validation of the proposed model through history-matching, the sensitivity analysis of the proposed model on gas production is conducted. This study reveals that the proppant size has a dominant influence. Although proppant with larger grain sizes leads to a more permeable propped fracture, it is found that only proppant grains of proper size, not too large or too small, has the potential to achieve economic gas production due to the combined effects of size effect of the grains and “bridging out” of the proppant. The second influential factor on the gas production is the proppant concentration which is followed by the viscosity of shale formation, the Young's modulus of proppant, and the Young's modulus of shale formation. This study leads to a better understanding of proppant-related mechanisms involved in hydraulic fracturing and gas production and provides an efficient numerical tool for the prediction of well performance in field development planning.

1. Introduction

With the increasing importance of clean energy, the development of shale gas is playing a more and more prominent role in satisfying the demand for gas in the future. Unlike conventional reservoirs that are easy to develop, advanced technologies, such as horizontal completions and hydraulic fracturing, are necessary to effectively extract gas from shale formations with extremely low matrix permeability. During hydraulic fracturing, the fluid containing proppants is pumped through the horizontal wellbore into fractures to prevent fractures from closing after the dissipation of fluid pressure. Both numerical studies and field evidence show that selection of proppant (including proppant type, size,

amount, etc.) according to reservoir properties plays an essential role in enhancing fracture conductivity and obtaining economic gas production rate (Economides and Martin, 2007; Tomac and Gutierrez, 2013; Yu et al., 2015). Consequently, it has vast importance to study the influences of proppant-related factors, including size, physical properties, and concentration of proppant on shale gas production.

There are several mechanisms that regulate shale gas production and production decline rate. This topic has been comprehensively investigated by Wang (2016). The main mechanisms include gas desorption (Yu and Sepehrnoori, 2014), matrix apparent permeability and its evolution (Javadpour, 2009; Wang and Marongiu-Porcu, 2015), natural fractures and fracture network (Aybar et al., 2014), stress-dependent

E-mail address: shifang@hyit.edu.cn.<https://doi.org/10.1016/j.petrol.2021.108523>

Received 18 May 2020; Received in revised form 10 January 2021; Accepted 6 February 2021

Available online 11 February 2021

0920-4105/© 2021 Elsevier B.V. All rights reserved.

conductivity (Cho et al., 2013), effect of water flowback (Cao et al., 2017), and so on. In addition, proppant-related factors have a significant influence on well performance of shale reservoir (Wang, 2016; Yu and Sepehrnoori, 2014; Yu et al., 2015). A large number of studies have shown that desirable conductivity of the propped fracture plays a crucial role in achieving economic gas production. The conductivity is directly related to the propped fracture width, which is affected by factors (Awoleke et al., 2012; Fredd et al., 2001; Lacy et al., 1997; Li et al., 2015) such as in-situ stresses, proppant size, mechanical parameters of proppant and formation, proppant concentration of the injected slurry. When the pumping process is done, the propped fracture width will decrease as a result of the proppant deformation, embedment, crushing, and shale creep (Lacy et al., 1997; Li et al., 2015; Zhang, 2014) in the presence of the closure stress. During the process of flowback and gas production, the increase of closure stress due to the decrease of reservoir pressure may further reduce the propped fracture width. Additionally, the proppant distribution in hydraulic fractures shows a significant influence on well performance (Cipolla et al., 2009; Yan et al., 2020; Yu et al., 2015). Thus, the process of proppant transport through the hydraulic fracture should be properly simulated in order to obtain a practical proppant distribution, instead of a uniform proppant distribution as assumed by most reservoir modeling works in the literature (Seales et al., 2016; Yu and Sepehrnoori, 2013). On the other hand, numerous studies (Chang and Zoback, 2009; Huang and Ghassemi, 2013; Li and Ghassemi, 2012; Sone and Zoback, 2014; Warpinski, 1989) have concluded that some kinds of shale exhibits pronounced viscous creep behavior, especially for the shale reservoir with high clay content. One of the consequences of the creep behavior is that proppant grains embedded gradually into the wall of hydraulic fracture, thus causing the decrease of fracture width and the reduction of gas production over time (Huang and Ghassemi, 2013; Zhang, 2014). On the other side, the rock creep, which is a time-dependent geomechanical behavior, impacts the permeability of the shale reservoir and hence affect the deliverability during the long gas production process (Huang and Ghassemi, 2013). Therefore, the creep of surrounding rock needs to be properly considered.

Due to the importance of proppant-related problems in hydraulic fracturing and gas production, some numerical studies have been performed by researchers. Ouyang et al. (1997) performed a numerical simulation using the adaptive finite element method to investigate the transportation and distribution process of proppant in the hydraulic fracture. Based on the displacement discontinuity method (DDM) (Crouch and Starfield, 1990), Weng et al. (2011) proposed a numerical model together with a proppant transport model to simulate the growth of the complex fracture network in consideration of proppant transport. By using the finite volume method (FVM) in conjunction with the finite difference method (FDM), Zhou et al. (2014) proposed a simulator considering propagation and closure of hydraulic fracture as well as proppant transport, and found that there is not enough proppant to prevent the fracture from closing at the perforation if the length is not quite short. Dontsov and Peirce (2015) built a hydraulic fracturing simulator that is able to describe the proppant behaviors including gravitational settling and tip screen-out, and in their model a width restriction based on the grain size is imposed to prohibit the grains from reaching the fracture tips. Kong et al. (2015) built a numerical approach considering proppant transport and studied the influence of some crucial parameters on the performance of hydraulic fracturing, and it's suggested that for the sake of improving the reservoir stimulation performance, the permeability of reservoir should be carefully considered for the selection of proppant size and pumping schedule. Yu et al. (2015) performed numerical studies on the influence of the uneven distribution of proppant on the performance of shale gas well. They (Yu et al., 2015) concluded that the shale gas desorption and the geomechanics effect play a critical role in gas production, and the proppant distribution can dramatically reduce the well performance. Han et al. (2016a) established a numerical model and studied the process of proppant failure,

and concluded that proppant grains near the wellbore are more likely to be crushed. Han et al. (2016b) established a CFD model in three-dimension and performed the simulation of proppant transport within fracture geometries including T-junction and crossing junction, and revealed that a higher pumping rate is beneficial to transport proppant through fracture junctions to reach further in fractures. Shiozawa and McClure (2016) simulated proppant transport in consideration of tip screen-out, fracture closure as well as proppant settling caused by the gravity, and sensitivity analysis indicates that reasonable results can be obtained without excessive mesh refinement. As stated above, these studies mainly focus on proppant transport and placement during the hydraulic fracturing stage, but not on stress-dependent conductivity changing of the propped fracture during the long-term gas production stage. Besides, proppant embedment due to shale creep or proppant crushing due to high closure pressure, which could be vital for production forecasting, has been seldom reported in the literature. More importantly, the strength of proppant is closely linked to its size. Specifically speaking, increasing the grain size will reduce its strength (Economides and Martin, 2007; Huang et al., 2014). Therefore, to gain a more comprehensive understanding of the factors responsible for production rate change, it is necessary to develop a more effective and sophisticated numerical model to simulate the process of hydraulic fracturing to obtain a practical proppant distribution (rather than a hypothetical uniform distribution as reported in the literature (Wang, 2016)), and then simulate the long-term process of gas production considering the resultant change of propped fracture conductivity.

The extended finite element method was firstly reported in 1999 (Belytschko and Black, 1999; Moës et al., 1999) and has been shown to be a very powerful numerical tool for the simulation of fracture or crack-related problems. By using this method, remeshing of finite element models is not necessary to track the fracture path during the fracture process. In the XFEM, the discontinuous surfaces are simulated through enriched degrees of freedom (DOFs) added on nodes around fractures. Seeing the convenience of the XFEM, many scholars have employed it to study hydraulic-fracturing-related problems including fluid-solid coupling mathematical models (Gordeliy and Peirce, 2013a, 2013b; Lecampion, 2009), hydraulic fracturing simulation inside the porous media (Mohammadnejad and Khoei, 2013), interactions between induced hydraulic fractures and natural fractures, as well as interactions between hydraulic fractures (Dahi-Taleghani and Olson, 2011; Khoei et al., 2015, 2016; Taleghani and Olson, 2014). Due to the extreme significance of proppant, in our previously published work (Shi et al., 2018), we proposed a new approach to obtain the conductivity of propped fractures using the XFEM considering proppant behaviors including transport and placement, deformation and embedment, as well as crushing, and this model has been verified by comparison with experimental data. In this study, in order to more accurately perform production forecasting in a long-time range, the viscoelasticity model describing the width evolution of propped fracture over time considering the creep behavior of surrounding rock is considered on the basis of our previous work (Shi et al., 2017, 2018).

In the presented paper, a sophisticated numerical model is proposed to perform the hydraulic fracturing simulation, which is followed by the reservoir simulation to forecast long-term gas production from shale. In the hydraulic fracturing simulation, some critical physical processes including single-phase flow and leak-off of the pumped fluid, deformation of surrounding rock media, fracture propagation, and proppant transport are all considered to obtain the distribution of proppant, which is then used in the subsequent reservoir simulation. A coupled deformation and two-phase flow model considering stress-dependent fracture conductivity, crushing of proppant grains, creep of surrounding rock, flowback of fracturing fluid, gas diffusion and desorption, and influence of natural fractures is developed to perform the reservoir simulation. The shut-in and the flowback of fracturing fluid are key processes that significantly influence the stress field around the fracture and thus the fracture width (Taleghani et al., 2020). Therefore, the fracture closure

during the shut-in and flowback processes is considered in this study. Based on the proposed model verified through history-matching, we conduct a sensitivity analysis of some factors on shale gas production, including size of proppant, Young's moduli and Poisson's ratios of proppant grains and shale formation, concentration of injected proppant, and viscosity of the shale formation.

The outline of the manuscript is structured as follows. The problem formulation and solution strategy including the governing equations, the extended finite element method, the mathematical description of the propped fracture, as well as mechanical models of proppant crushing and shale creep are presented in Section 2. The base case simulation as well as history-matching with field data in both Marcellus shale and Barnett shale are given in Section 3. The sensitivity analysis is performed in Section 4 and conclusions are presented in Section 5.

2. Problem formulation and solution strategy

As shown in Fig. 1, a two-phase (fluid and gas) porous media (Ω in two dimensions) contains a hydraulic fracture Γ_{HF} full of incompressible fluid at high-pressure and a fracture Γ_{PF} propped by proppant grains. The boundary of Ω is Γ which has an outward normal vector \mathbf{n}_Γ . The external force $\bar{\mathbf{t}}$ and the specified displacements (zero in most cases) $\bar{\mathbf{u}}$ are respectively applied on Γ_t and Γ_u . The fluid pressure on Γ_{pw} is \bar{p}_w . The capillary pressure on Γ_{pc} is \bar{p}_c . The volume out-fluxes of fluid phase and gas phase applied on Γ_{qw} and Γ_{qg} are \bar{q}_w and \bar{q}_g , respectively. The fracture surfaces are denoted by the “+” and the “-” signs. To depict the slurry flow along the hydro-fracture, a curvilinear coordinate system s in one-dimension is defined.

The following assumptions are made in deriving the model: (1) The slurry is assumed as a Newtonian fluid (Adachi et al., 2007; Hammond, 1995; Tomac and Gutierrez, 2013). (2) The fracture propagation is regarded as quasi-static (Adachi et al., 2007). (3) There is no fluid lag between the fluid front and the tip of hydraulic fracture. (4) The shale formation behaves as a brittle material. (5) Proppant settling due to gravity (Shi et al., 2018), proppant flowback and proppant diagenesis (Yu and Sepehrnoori, 2014; Yu et al., 2015) are ignored. (6) The Klinkenberg effect (gas-slippage effect) (Klinkenberg, 1941) and the non-Darcy effect (Liu et al., 2016a) have not been considered, because it is not the focus of this work. (7) The natural fractures are not explicitly involved in the hydraulic fracturing simulation, but the permeability enhancement caused by natural fractures is considered in the reservoir

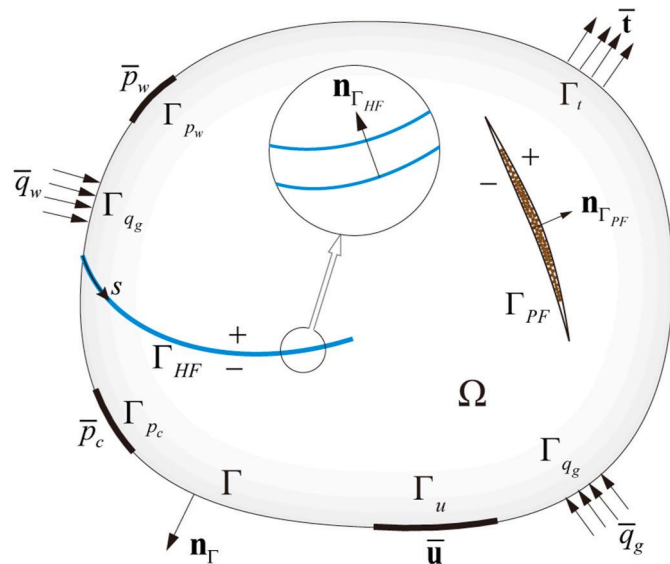


Fig. 1. Sketch of a porous media which contains a hydraulic fracture and a propped fracture.

simulation.

2.1. Governing equations

Without considering the body force, the equilibrium equation of the quasi-static problem within domain Ω can be written as

$$\nabla \cdot \boldsymbol{\sigma} = \mathbf{0} \quad \text{in } \Omega \quad (1)$$

in which $\boldsymbol{\sigma} = \boldsymbol{\sigma}' - \alpha p \mathbf{I}$ represents the Cauchy stress tensor. $\boldsymbol{\sigma}'$ represents the effective stress, p is the reservoir pressure, α is the Biot constant, and \mathbf{I} is the identity tensor. p can be expressed as $p = S_w p_w + S_g p_g$, where S_w , S_g , p_w , p_g are fluid saturation, gas saturation, fluid pressure, gas pressure, respectively. Using equations $S_w + S_g = 1$ and $p_w = p_g - p_c$, the reservoir pressure P can be further written as

$$p = p_g - S_w p_c \quad (2)$$

In this paper, the capillary pressure is calculated according to the following equation (Cui et al., 2020)

$$p_c = p_e S_e^{-1/\lambda} \quad (3)$$

where the entry pressure p_e and the parameter λ related to the pore size distribution are taken as 0.1 MPa and 2, respectively (Cui et al., 2020; Wei et al., 2020); S_e represents the effective saturation and takes the following form

$$S_e = \frac{S_w - S_{wr}}{1 - S_{wr} - S_{gr}} \quad (4)$$

in which S_{wr} and S_{gr} represent the saturation of residual fluid and gas, respectively. The boundary conditions of Eq. (1) can be written as

$$\begin{cases} \mathbf{u} = \bar{\mathbf{u}} & \text{on } \Gamma_u \\ \boldsymbol{\sigma} \cdot \mathbf{n} = \mathbf{t} & \text{on } \Gamma_t \\ \boldsymbol{\sigma} \cdot \mathbf{n}_{\Gamma_{HF}} = -\alpha p \mathbf{n}_{\Gamma_{HF}} & \text{on } \Gamma_{HF} \\ \boldsymbol{\sigma} \cdot \mathbf{n}_{\Gamma_{PF}} = \mathbf{t}^{propped} - \alpha p \mathbf{n}_{\Gamma_{PF}} & \text{on } \Gamma_{PF} \end{cases} \quad (5)$$

where $\mathbf{t}^{propped}$ represents the traction force caused by the interaction between the proppant and the surfaces of propped fracture. The deformation of the shale matrix follows a linear relationship $\boldsymbol{\sigma}' = \mathbf{D} : \boldsymbol{\varepsilon}$, where \mathbf{D} and $\boldsymbol{\varepsilon}$ represent the elasticity matrix of moduli and mechanical strain, respectively.

The immiscible two-phase flow follows the mass conservation law (Wei et al., 2020)

$$\frac{\partial m_\chi}{\partial t} - \nabla \cdot \left(\mathbf{k} \rho_\chi \frac{k_{r\chi}}{\mu_\chi} \nabla p_\chi \right) = Q_\chi \quad (6)$$

where subscript χ equals w and g for the fluid phase and gas phase, respectively; m_χ represents the mass content per unit volume; ρ_χ , $k_{r\chi}$, μ_χ , and Q_χ , represent the density, relative permeability, viscosity, and source or sink term, respectively; \mathbf{k} is the permeability vector; t denotes time. The fluid content m_w can be written as (Ma et al., 2017)

$$m_w = S_w \rho_w \phi \quad (7)$$

where ϕ is the porosity. There are two different sources contribute to gas content m_g

$$m_g = S_g \rho_g \phi + m_{ga} \quad (8)$$

where $\rho_g \phi$ corresponds to the free-gas, m_{ga} corresponds to the adsorbed gas. The Langmuir isothermal is a widely used model to describe the physical process of gas adsorption and desorption (Yu and Sepehrnoori, 2014). m_{ga} can be obtained by using the Langmuir equation (Langmuir, 1918).

$$m_{ga} = (1 - \phi) \rho_r \rho_g^{st} \frac{V_L p_g}{p_g + p_L} \quad (9)$$

where ρ_r is the density of shale formation, ρ_g^{st} represents the density of gas under standard conditions, V_L is the Langmuir volume per unit mass of shale and p_L is the Langmuir pressure. The relative permeabilities of fluid and gas are calculated by (Cui et al., 2020; Ma et al., 2017)

$$k_{rw} = \sqrt{S_e} \left(1 - (1 - S_e^{1/m})^m \right)^2 \quad (10)$$

$$k_{rg} = (1 - S_e)^2 (1 - S_e^2) \quad (11)$$

in which the pore size distribution index m is taken as 0.5 (Cui et al., 2020) in this paper. Because the pore pressure is changing all the time during the gas production process, the shale gas density changes according to the ideal gas law (Cao et al., 2017)

$$\rho_g = \frac{M_g}{RT} p_g = \frac{p_g}{p^{st}} \rho_g^{st} \quad (12)$$

where R , M_g , and p^{st} denote the universal gas constant, the molecular weight of gas, and the standard atmospheric pressure, respectively.

In this paper, the seepage in the shale formation as well as the hydraulic fracture is solved as a whole, thus the fluid exchange between the fracture and the surrounding (fluid leak-off) can be obtained as a direct results of the coupled system (Cheng et al., 2019). For the hydraulic fracture, the permeability vector \mathbf{k} takes the form $\mathbf{k} = [k_f^n \ k_f^t]$, where k_f^n and k_f^t are the normal and tangential permeability of the hydraulic fracture, respectively. The normal permeability k_f^n of the fracture is taken as the permeability of the shale formation in order to consider the fluid leak-off process (Cheng et al., 2019). For a fluid-filled hydraulic fracture, $k_f^n = w^3/12$ in which w denotes the fracture width. For a propped hydraulic fracture, the tangential permeability k_f^t of the hydraulic fracture will be presented in Section 2.3. For isotropic and homogeneous shale formations, \mathbf{k} can be treated as a scalar quantity k . It should be noted that because of the small pore diameters of shale gas reservoirs, the effect of the Knudsen diffusion (Jiang and Younis, 2015) is considered using the apparent permeability correction method proposed by Florence et al. (2007):

$$k_{app} = (1 + \alpha_k K_n) \left(1 + \frac{4K_n}{1 + K_n} \right) k \quad (13)$$

where α_k takes the following form

$$\alpha_k = \frac{128}{15\pi^2} \tan^{-1} (4K_n^{0.4}) \quad (14)$$

and K_n is the Knudsen number

$$K_n = \frac{\mu_g}{2.81708p} \sqrt{\frac{\pi RT}{2M_g}} \frac{\phi}{k} \quad (15)$$

Natural fractures play an important role in the hydraulic fracturing process. In this paper, we define the enhanced permeability area (EPA) (Liu et al., 2019) caused by the tensile and shear failure of natural fractures induced by the hydraulic fracture, and the following failure model is proposed to determine the EPA.

$$\begin{cases} f_1 = \sigma_3 + S_T \\ f_2 = 2c_s \frac{\cos \varphi}{1 - \sin \varphi} + \sigma_3 \frac{1 + \sin \varphi}{1 - \sin \varphi} - \sigma_1 \end{cases} \quad (16)$$

where S_T , c_s , and φ are the tensile strength, cohesive strength, and friction angle of the rock formation containing natural fractures, respectively. σ_1 and σ_3 represent the maximum and minimum principal stresses, respectively. f_1 and f_2 are calculated at the Gauss points of elements. A tensile fracturing occurs if $f_1 < 0$, and a shear fracturing

occurs if $f_2 < 0$. The permeability of the EPA can be written as $k_{EPA} = \zeta k_{app}$, where ζ is the enhancement coefficient and taken as 10 (Clarkson et al., 2015) in this paper.

After combining the equations presented above, the fluid and gas flow equations can be derived as follows, respectively

$$\rho_w S_w \frac{\partial \phi}{\partial t} + \rho_w \phi \frac{\partial S_w}{\partial t} - \nabla \cdot \left(\rho_w \frac{k_{app} k_{rw}}{\mu_w} \nabla p_w \right) = Q_w \quad (17)$$

$$\rho_g S_g \frac{\partial \phi}{\partial t} + \rho_g \phi \frac{\partial S_g}{\partial t} + \left(\rho_r \rho_g^{st} \frac{V_L p_L}{(p_g + p_L)^2} + \frac{S_g \phi M_g}{RT} \right) \frac{\partial p_g}{\partial t} - \nabla \cdot \left(\rho_g \frac{k_{app} k_{rg}}{\mu_g} \nabla p_g \right) = Q_g \quad (18)$$

By combining the mass conservation equation and the Poiseuille's law, we can write the flow equation of proppant (Adachi et al., 2007) within the hydraulic fracture as

$$\frac{\partial(cw)}{\partial t} - \frac{\partial}{\partial s} \left(\frac{w^3}{12\mu(0)} f_p \frac{\partial p_w}{\partial s} \right) - c_{inj}(t) Q_{inj} \delta(s) = 0 \quad (19)$$

where w denotes the fracture width, c represents the proppant volumetric concentration, $\delta(\cdot)$ denotes the Dirac-delta function, and $c_{inj}(t)$ is the concentration in volume of proppant at the pumping point. It is important to point out that if the proppant has a larger size in diameter than the fracture width, it will be prevented from flowing through the narrow part of the hydro-fracture, for example, the region near the tip. In Eq. (19), f_p takes the form $f_p = \frac{2\mu(0)}{3\mu(c)} c$ (Shi et al., 2016), in which $\mu(c)$ represents the effective viscosity and can be written as

$$\mu(c) = \mu(0) \left(1 - \frac{c}{\hat{c}} \right)^{\hat{m}} \quad (20)$$

in which the saturation concentration \hat{c} and the exponent \hat{m} are chosen as 0.6 and 1.05 (Adachi et al., 2007; Shi et al., 2016), respectively, in this paper. The above flow equation of the proppant is solved by using the finite difference method, details can be found in our previous work (Shi et al., 2016).

2.2. Extended finite element method

For a point \mathbf{x} in Ω , its displacement \mathbf{u} takes the following form according to the extended finite element method (Khoei, 2014)

$$\mathbf{u}(\mathbf{x}) = \sum_{I \in N_{all}} N_I^u(\mathbf{x}) \mathbf{u}_I + \sum_{I \in N_{frac}} N_I^u(\mathbf{x}) H(\mathbf{x}) \mathbf{a}_I + \sum_{I \in N_{tip}} N_I^u(\mathbf{x}) \sum_{l=1}^4 F_l(\mathbf{x}) \mathbf{b}_I^l \quad (21)$$

where N_{all} represents the set of all nodes, N_I^u is the regular finite element shape function. N_{frac} is the set of nodes enriched with the Heaviside function $H(\mathbf{x})$. N_{tip} is the set of nodes enriched with the crack-tip function $F_l(\mathbf{x})$ ($l = 1, 4$). Vector \mathbf{u}_I contains the regular DOFs of node I and vectors \mathbf{a}_I , \mathbf{b}_I^l ($l = 1, 4$) contain the enriched DOFs of node I . $H(\mathbf{x})$ equals 1 on one side of the fracture and equals -1 on the other side. $F_l(\mathbf{x})$ takes the following form for brittle materials

$$\{F_l(r, \theta)\}_{l=1}^4 = \left\{ \sqrt{r} \sin \frac{\theta}{2}, \sqrt{r} \cos \frac{\theta}{2}, \sqrt{r} \sin \theta \sin \frac{\theta}{2}, \sqrt{r} \sin \theta \cos \frac{\theta}{2} \right\} \quad (22)$$

in which (r, θ) denotes the polar coordinates originating from the fracture tip.

For the hydraulic fracture in a porous media, the pressure across the fracture is continuous, but the flow rate across the fracture, i.e., derivative of the pressure, is discontinuous. For a point \mathbf{x} in Ω , its pressure \mathbf{p} takes the following form according to the extended finite element method (Liu et al., 2016b):

$$\mathbf{p}(\mathbf{x}) = \sum_{I \in N_{all}} N_I^p(\mathbf{x}) \mathbf{p}_I + \sum_{I \in N_{frac}} N_I^p(\mathbf{x}) A(\mathbf{x}) \mathbf{c}_I + \sum_{I \in N_{tip}} N_I^p(\mathbf{x}) \sum_{l=1}^3 B_l(\mathbf{x}) \mathbf{d}_I^l \quad (23)$$

where N_l^p is the regular finite element shape function. N_{frac} is the set of nodes enriched with the absolute signed distance function $A(\mathbf{x}) = |s(\mathbf{x})|$ in which $s(\mathbf{x})$ represents the signed distance of point \mathbf{x} to the fracture. N_{tip} is the set of nodes enriched with the crack-tip function $B_l(\mathbf{x})$ ($l = 1, 3$). Vector \mathbf{p}_l contains the regular pressure DOFs of node l and vectors $\mathbf{c}_l, \mathbf{d}_l^l$ ($l = 1, 3$) contain the enriched pressure DOFs of node l . $B_l(\mathbf{x})$ takes the following form (Liu et al., 2016b):

$$\{B_l(r, \theta)\}_{l=1}^3 = \left\{ r \cos \frac{\theta}{2}, r^2 \cos \frac{\theta}{2}, \sqrt{r} \cos \frac{\theta}{2} \right\} \quad (24)$$

2.3. Width and permeability of propped fracture

As a matter of fact, the proppant grains are in different diameters. Nevertheless, it is very challenging to derive a mathematical model involving grains in different sizes. Therefore, it is assumed that all of the proppants are in the same diameter D_p , are depicted in Fig. 2. With the decrease of the fluid pressure inside the hydraulic fracture, the fracture width will decrease until the proppant pack takes effect and keeps the fracture open. A hexagonal close packing pattern is assumed for the arrangement of the proppant grains (Li et al., 2016), as depicted in Fig. 3. If the closure stress equals zero, then the propped fracture width $w_p^o(S)$ can be obtained according to $w_p^o(s) = w_o(s)c(s)/\eta$, where w_o (as depicted in Fig. 2) represents the fracture opening at the end of the pumping process. Before the proppant pack takes effect, the width of the hydraulic fracture can be calculated according to the following equation

$$w = 2n_{\Gamma_{nr}} \cdot \sum_{l \in N_{frac}} N_l^u(\mathbf{x}) \mathbf{a}_l + 2n_{\Gamma_{nr}} \cdot \sqrt{r} \sum_{l \in N_{tip}} N_l^u(\mathbf{x}) \mathbf{b}_l^l \quad (25)$$

The coefficient η is known as packing density (Steinhaus, 1999) related to the packing pattern and is equal to 0.74 in this study.

Afterwards, the fracture aperture will decline from w_p^o to w_p as a consequence of proppant deformation and embedment. Due to the combined factors such as roughness of the fracture surface, heterogeneity of the proppant grains, as well as the proppant volumetric concentration, the deformation of the proppant pack is complicated and practically impossible to be exactly described by means of simulation. Consequently, some theoretical assumptions and ideal conditions must be imposed to establish reasonable and simplified analytical models. In practice, the Hertzian contact theory (Johnson, 1985) has been extensively used in the literature (Li et al., 2015, 2016; Neto et al., 2015) when developing models to get the width or conductivity of fractures

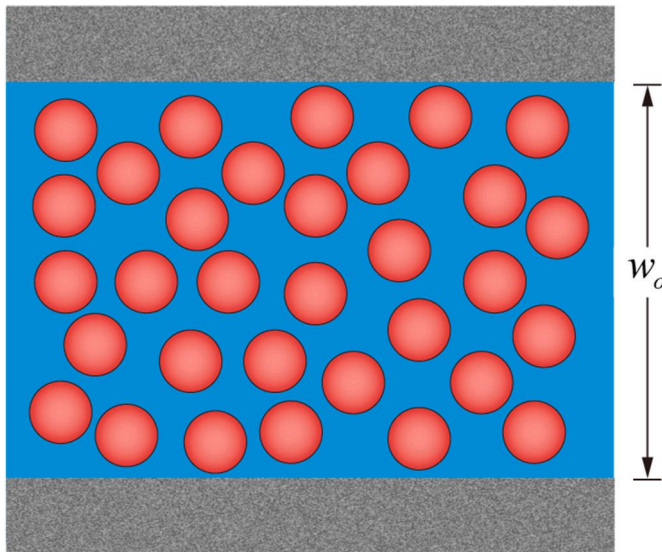


Fig. 2. Depiction of proppant grains in the hydraulic fracture when the pumping process is just finished.

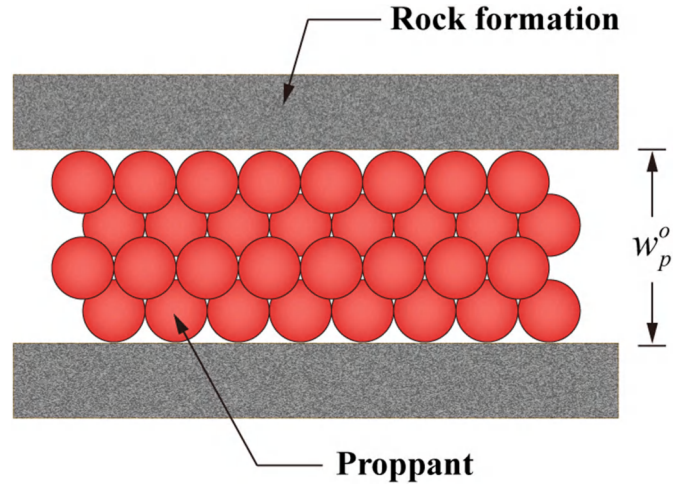


Fig. 3. Depiction of multilayer-packed proppant grains without closure stress.

filled with proppant. For example, a mathematical model used to determine w_p in consideration of elastic deformation and embedment of proppant was proposed by Li et al. (2016), which can be written as

$$w_p = w_p^o - 1.89D_p p_{closure}^{2/3} \left[(n_1 - 1)T_1^{2/3} + T_2^{2/3} \right] \quad (26)$$

where

$$\begin{cases} n_1 = \text{ceil} \left(0.986 \frac{w_p^o}{D_p} \right) \\ T_1 = \frac{1 - \nu_p^2}{E_p} \\ T_2 = \frac{1 - \nu_p^2}{E_p} + \frac{1 - \nu_r^2}{E_r} \end{cases} \quad (27)$$

In Eqs. (26) and (27), $\text{ceil}(x)$ is the ceiling function and n_1 is the number of layers of proppant; $p_{closure}$ represents the closure stress; E_r and E_p represent Young's modulus; ν_r and ν_p represent Poisson's ratio; The subscripts r and p represent shale formation and proppant grains, respectively.

Based on Eq. (26), Li et al. (2016) proposed the permeability of propped fracture which takes the following form (readers are referred to (Li et al., 2016) for a detailed derivation)

$$k_f^r = 0.07 \left(0.078D_p - 0.605D_p p_{closure}^{2/3} T_1^{2/3} \right)^2 \times \left\{ 1 - \frac{\frac{\pi}{3}ND_p^3 - \frac{\pi}{4}D_p^3 p_{closure}^{4/3} T_3 + \frac{\pi}{4}D_p^3 p_{closure}^2 T_4}{\left\{ w_p^o - 1.89D_p p_{closure}^{2/3} \left[(n_1 - 1)T_1^{2/3} + T_2^{2/3} \right] \right\} \times 10^2} \right\} \quad (28)$$

in which

$$\begin{cases} N = \text{ceil} \left(0.986 \frac{w_p^o}{D_p} \right) n_2 \\ T_3 = 6.5(N - n_2)T_1^{4/3} + 7.15n_2T_2^{4/3} \\ T_4 = 2.25(N - n_2)T_1^{4/3} + 4.5n_2T_2^{4/3} \\ n_2 = \frac{2}{\sqrt{3}D_p} \times 10^2 \end{cases} \quad (29)$$

2.4. Proppant crushing and shale creep

The proppant crushing plays a significant role in the reduction of the conductivity of propped fracture (Seales et al., 2016; Wang, 2016) and it should be properly reflected in the simulation. The plastic behavior of

proppant has not been considered in this paper because the failure of proppant grains is a sudden process, but not a gradually changing plastic deformation process (Ouwkerk, 1991; Zhang et al., 1990). On the other side, there are generally three kinds of failure modes for brittle material, i.e., tension failure, compression failure, and shear failure. In this study, we assume that the principal failure mode of proppant grains is tension failure which is in accordance with the contact model proposed by Li et al. (2016). We have performed the numerical simulation based on the compression failure criterion. However, the obtained fracture widths are much wider than the experimental results, because the compressive strength of proppant is ordinarily larger than the tensile one. Besides, the shear failure is not a common failure mode of proppant packing (Osholake et al., 2013; Ouwkerk, 1991), no matter in the simulation aspect or the experimental aspect. Therefore, compression failure and shear failure have not been taken into account. It is assumed in this paper that tensile stresses exceeding the tensile strength will cause the failure of grains (Johnson et al., 1973). Consider the elastic contact between spheres, the external force F applied on spheres can be obtained as $F = D_p^2 p_{closure} \sqrt{3}/2$ (Li et al., 2016). Then, the radial stress σ_r in tension within the contact circle can be written as (Johnson, 1985)

$$\sigma_r = p_m \left\{ \frac{1 - 2\nu_p}{3} \left(\frac{a^2}{r^2} \right) \left[1 - \left(1 - \frac{r^2}{a^2} \right)^{3/2} \right] - \left(1 - \frac{r^2}{a^2} \right)^{1/2} \right\}, r \leq a \quad (30)$$

in which a represents the contact circle radius and

$$a = \left[\frac{3}{8} F D_p \left(\frac{1 - \nu_p^2}{E_p} \right) \right]^{1/3} \quad (31)$$

In Eq. (30), p_m represents the maximum contact pressure and

$$p_m = \frac{3F}{2\pi a^2} \quad (32)$$

Then, the maximum tensile stress, in other words, the maximum value of the radial stress, can be expressed as

$$\sigma_t = \sigma_r|_{r=a} = \frac{p_m(1 - 2\nu_p)}{3} \quad (33)$$

Finally, combing Eqs. (31)–(33) yields

$$\sigma_t = \frac{(\sqrt{3} p_{closure}/2)^{1/3} (1 - 2\nu_p)}{2\pi \left[\frac{3}{8} \left(\frac{1 - \nu_p^2}{E_p} \right) \right]^{2/3}} \quad (34)$$

Because of the immense complexity, it is still a challenging task to depict the fracture width changing as well as the conductivity changing after proppant failure. The theory of damage has been successfully applied to study the breakage process of granular materials for many years (Gambarotta and Lagomarsino, 1993; Sokolinsky et al., 2011). Thus, a damage model is suggested here

$$\omega = \begin{cases} 0, & 0 < \sigma_t < \sigma_t^f \\ \frac{\sigma_t^u (\sigma_t - \sigma_t^f)}{\sigma_t (\sigma_t^u - \sigma_t^f)}, & \sigma_t^f \leq \sigma_t < \sigma_t^u \end{cases} \quad (35)$$

in which ω denotes the damage factor and $0 \leq \omega \leq 1$, σ_t^f represents the tensile stress at the moment the grains start to fail, σ_t^u is the tensile stress when the grains are totally cracked. Using the above damage model, the permeability of the propped fracture can be written as $\tilde{k}_f^\tau = (1 - \omega)k_f^r$ (Seales et al., 2016).

It is well known that, as the closure stress increases, the conductivity of proppants of larger sizes is smaller than the conductivity of smaller proppants (Economides and Martin, 2007), namely, the grain strength shows a pronounced size effect in a way that smaller grains require higher stress to activate cracking (Huang et al., 2014). The following

equation is proposed to consider the size effect (Shi et al., 2018):

$$\sigma_t^f = \sigma_t^o \left(\frac{V}{V_o} \right)^{-1/\kappa} \quad (36)$$

where σ_t^o denotes the proppant strength in unit volume V_o , and κ represents the Weibull's modulus which equals 11 in this paper (Shi et al., 2018; Tsoungui et al., 1999).

As discussed in the introduction, the viscoelastic and creep of shale formation can reduce the conductivity of proppant pack during the life of a well (Wang, 2016; Zhang, 2014). The Kelvin-Voigt model (Chu and Chang, 1980; Marques and Creus, 2012) consisting of a viscous damper (of viscosity factor η) and a linear spring (of Young's modulus E) in parallel connection is adopted to describe the creep behavior of the shale formation. Therefore, the linear elastic constitutive of the shale formation should be replaced with a corresponding viscoelastic one (Huang and Ghassemi, 2013). According to the Kelvin-Voigt model, the total stress is calculated by summing the stress in the viscous damper and the stress in the linear spring, that is, $\sigma(t) = E\varepsilon + d\varepsilon/dt$. Thus, the strain can be obtained as

$$\varepsilon(t) = \frac{\sigma(t)}{E} \left[1 - \exp\left(-\frac{t}{\eta/E}\right) \right] \quad (37)$$

Finally, the effects of shale creep on the width of the propped fracture can be considered by replacing E_r in Eq. (27) with E_r^c

$$E_r^c = \frac{E_r}{1 - \exp\left(-\frac{t}{\eta_r/E_r}\right)} \quad (38)$$

2.5. Solution strategies

As shown in Fig. 4, the solution procedure is divided into two successive stages, i.e., the hydraulic fracturing stage, and the flowback and gas production stage. In the first stage, a single-phase flow model is adopted and the gas phase remains constant. In the second stage, a two-phase flow model is adopted (Zhang et al., 2017). Within each time step of the hydraulic fracturing stage, Eqs. (1), (17) and (19) are solved. Firstly, the solution of the nonlinear fluid-solid coupled system (Eqs. (1) and (17)) is obtained iteratively by applying the Newton's method (Press et al., 1992). Then, Eq. (19) which describes the transportation of proppant is solved to get the proppant concentration $c(s)$ using the upwind method with a second-order correction (Adachi et al., 2007; Shi

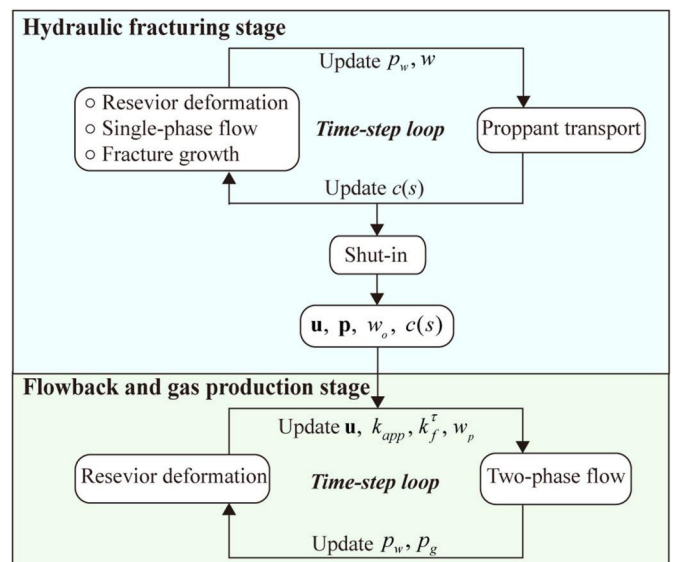


Fig. 4. Flow chart of the solution procedure.

et al., 2016). After the hydraulic fracturing simulation, the shut-in period is modeled by solving Eqs. (1) and (17) using the Newton's method. In the flowback and gas production stage, the equilibrium equation (Eq. (1)) describing the reservoir deformation and coupled partial differential equations of the two-phase flow model (Eqs. (17) and (18)) are iteratively solved, during which the reservoir pressure p , fracture width w_p , reservoir permeability k_{app} , and fracture permeability k_f^* are updated within each time-step loop. During the solution process of the early flowback and gas production stage, special attention should be paid to the calculation of the fracture width. With the decrease of fluid pressure, the proppant pack will take effect and keep the fracture open. Therefore, within each time step, if the fracture width w is less than w_p^0 for any point along the hydraulic fracture, the fracture width should be recalculated according to Eq. (26) instead of Eq. (25).

3. Base case simulation and history-matching

The numerical model presented in this paper has been implemented in an in-house program called PhiPsi (visit <http://phipsi.top> for details). This program allows us to investigate which factors have the most influence on the global well performance by explicitly considering some key physical processes during the hydraulic fracturing stage and the subsequent flowback and gas production stage. In this section, we attempt to validate the proposed numerical model by performing the history-matching with field data in the literature from Marcellus shale (Yeager and Meyer, 2010) as well as Barnett shale (Grieser et al., 2009). In should be noted that data from Marcellus shale are used for the base case of the sensitivity analysis presented in the following Section 4.

It's assumed that hydraulic fracturing stages are evenly spaced along the wellbore and are symmetrical about the wellbore. Instead of establishing a complete and complex horizontal well model, a half-stage simulation model with symmetry boundary conditions (Wang, 2016) applied along the horizontal wellbore (as shown in Fig. 5) is adopted in this study. The total gas production can then be obtained by multiplying the production from the half-stage simulation model first by two and then by the total number of stages. There are 7 stages in the Marcellus shale case, and each stage contains 4 clusters with a spacing of 15.2 m (50 ft). The length L and the width W of the simulation model are 150.8 m (495 ft) and 61.0 m (200 ft), respectively (Yu and Sepehrnoori, 2013). As shown in Fig. 5, since all hydraulic fractures initiated from the perforation clusters within a fracturing stage are considered, the stress shadow effect between hydraulic fractures can be captured. In the Barnett shale case, however, the fracture spacing is much larger (30.5 m (100 ft)) (Yu and Sepehrnoori, 2014), the stress shadow effect can then be neglected (Yu and Sepehrnoori, 2014). Therefore, each simulation model contains only one cluster and there are 28 clusters in total. The length L and width W of the simulation model are 228.6 m (750 ft) and

30.5 m (100 ft), respectively (Yu and Sepehrnoori, 2014). In addition, the heights of the hydraulic fractures in the Marcellus shale case and Barnett shale case are 52.7 m (173 ft) and 91.4 m (300 ft), respectively. The numbers of elements for the hydraulic fracturing simulation are 8168 and 4786 for the Marcellus shale case and Barnett shale case, respectively. All other input parameters (Cui et al., 2020; Grieser et al., 2009; Liu et al., 2016a; Yeager and Meyer, 2010; Yu and Sepehrnoori, 2014; Yu et al., 2015) for both cases are summarized in Table 1.

The maximum circumferential tensile stress criterion (Erdogan and Sih, 1963; Shi et al., 2016) is used to predict the cracking of the shale. A constant net pressure of 2 MPa is applied on the initial hydraulic fracture of 3.0 m as the initial solution for the Newton's method. The calculations continue until the maximum half-length of fracture reaches 122 m (400 ft) and 47.2 m (155 ft) in the Marcellus shale case and Barnett shale case, respectively. The shut-in time for both cases is taken as 1 day (Zhang et al., 2017). Then, we run the flowback and gas production simulation for a period of 5 years. The curves of bottom hole pressure (BHP) used in this paper are shown in Fig. 6 according to the data reported in the literature (Mayerhofer et al., 2006; Pan and Connell, 2015; Yu and Sepehrnoori, 2014; Yu et al., 2015). The values of BHP after 9 months in the Marcellus case and in the Barnett shale case are taken as 2.44 MPa and 3.45 MPa, respectively (Pan and Connell, 2015; Yu and Sepehrnoori, 2014).

All simulations are performed on a computer with Intel i7-8700K 3.0 GHz processor and 32 GB memory. In this study, it takes 22.7 min and 12.2 min to perform the hydraulic fracturing for the Marcellus shale case and Barnett shale case, respectively. In addition, the CPU times consumed by the gas production simulation for a period of 5 years are 13.0 min and 6.2 min for the Marcellus shale case and Barnett shale case, respectively. What needs to be noted is that the Barnett shale case takes less time because only one hydraulic fracture is considered in the

Table 1
Parameters for the history-matching cases.

Parameter	Unit	Marcellus shale	Barnett shale
Young's modulus of formation, E_r	GPa	24.0	51.0
Poisson's ratio of formation, ν_r	—	0.2	0.2
Fracture toughness of formation, K_{IC}	MPa·m ^{1/2}	1.0	1.0
Tensile strength of formation, S_T	MPa	1.0	1.0
Cohesive strength of formation, c_s	MPa	3.0	3.0
Friction angle of formation, φ	degree	25	25
Reservoir temperature, T	°C	76.1	65.6
Young's modulus of proppant, E_p	GPa	20.0	20.0
Poisson's ratio of proppant, ν_p	—	0.2	0.2
Average proppant size, D_p	mm	0.6	0.6
Strength of proppant, $\sigma \sigma t$	MPa	80	80
Crushing strength of proppant, $\sigma u t$	MPa	1000	1000
Pumping rate, Q_{inj}	m ² /s	0.001	0.001
Pumping concentration of proppant, C_{inj}	—	0.3	0.3
Viscosity of injected fluid, μ	Pa·s	0.001	0.001
Biot's coefficient, α	—	0.8	0.8
Horizontal maximum stress, σ_H	MPa	50.0	30.0
Horizontal minimum stress, σ_h	MPa	47.0	27.0
Density of formation, ρ_r	kg/m ³	2460	2600
Langmuir volume, V_L	m ³ /kg	0.00566	0.00272
Langmuir pressure, P_L	MPa	3.45	4.48
Gas viscosity, μ_g	mPa·s	0.02	0.02
Gas density, $\rho_{st g}$	kg/m ³	0.533	0.533
Molecular weight of gas, M_g	kg/mol	0.016	0.016
Initial reservoir pressure, P_i	MPa	34.6	20.3
Initial formation permeability, k	m ²	6.0×10^{-19}	3.5×10^{-19}
Initial formation porosity, ϕ	—	0.046	0.06
Initial fluid saturation, S_w	—	0.1	0.2
Residual fluid saturation, S_{wr}	—	0.05	0.05
Residual gas saturation, S_{wg}	—	0.1	0.1
Viscosity coefficient of formation, η_r	Pa·s	0	0

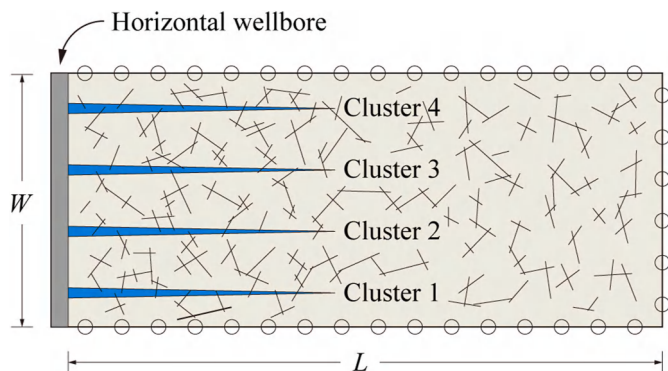


Fig. 5. A plane view of the half-stage simulation model containing four perforation clusters, “o” represents the no-flux boundary condition, and “—” represents natural fracture.

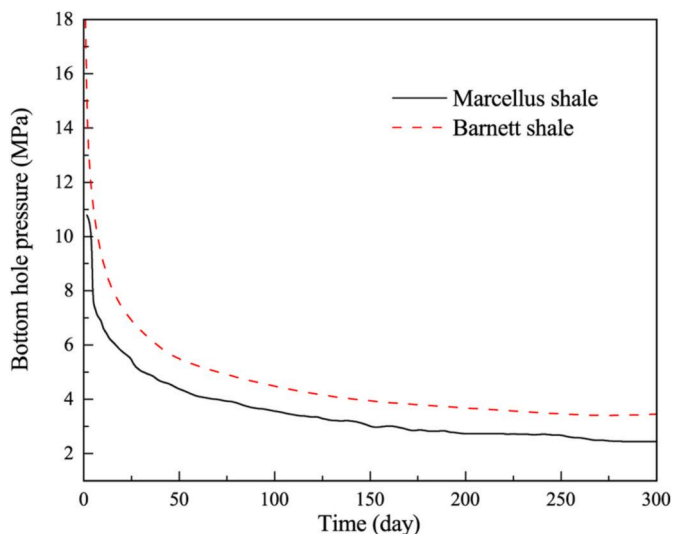


Fig. 6. Bottom hole pressure of the first 300 days used for history-matching.

simulation model. As a comparison, the hydraulic fracturing simulation of the Marcellus shale case is also carried out by using the conventional FEM in which mesh refinement is required after the propagation of hydraulic fractures. The computational methodology is the same as the XFEM-based model described in Section 2 except for the spatial discretization of the displacement field. The numbers of elements at the first and last time steps are 4236 and 8046, respectively. The total consumed CPU time is 40.9 min and is about 80% more than that consumed by using the XFEM. It can be concluded that the FEM shows much lower computational efficiency than XFEM in which the time-consuming mesh refinement process and the resulting data mapping between non-matching meshes are avoided.

For the Marcellus shale case, the log/log graph of the evolution of fracture width at the injection point of cluster 1 is presented in Fig. 7, in which t_1 (583 s) represents the time at the end of the hydraulic fracturing stage, t_2 (1 day) represents the time at the end of the shut-in period, and t_3 (2.4 days) represents the time when the proppant pack takes effect to keep the hydraulic fracture open. Besides, the fracture openings at t_1 , t_2 , and t_3 are shown in Fig. 8. The closure behavior of the

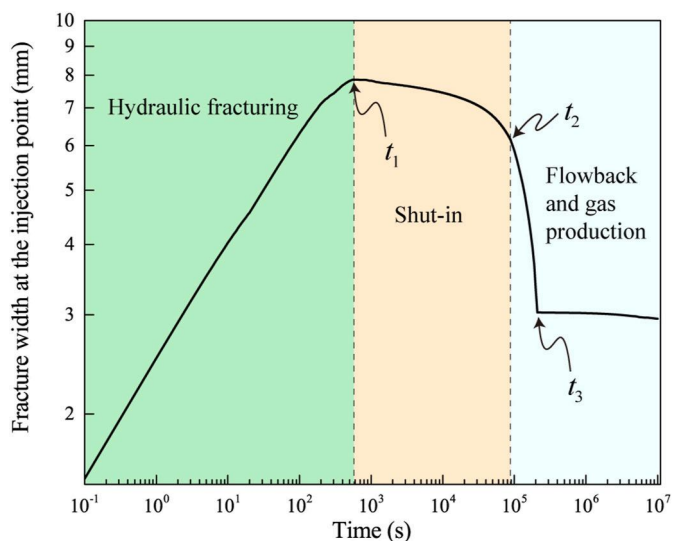


Fig. 7. Log/log graph of the evolution of fracture width at the injection point of cluster 1 for the Marcellus shale case. t_1 is the time at the end of the hydraulic fracturing stage. t_2 is the time at the end of the shut-in period. t_3 is the time when the proppant pack takes effect to keep the hydraulic fracture open.

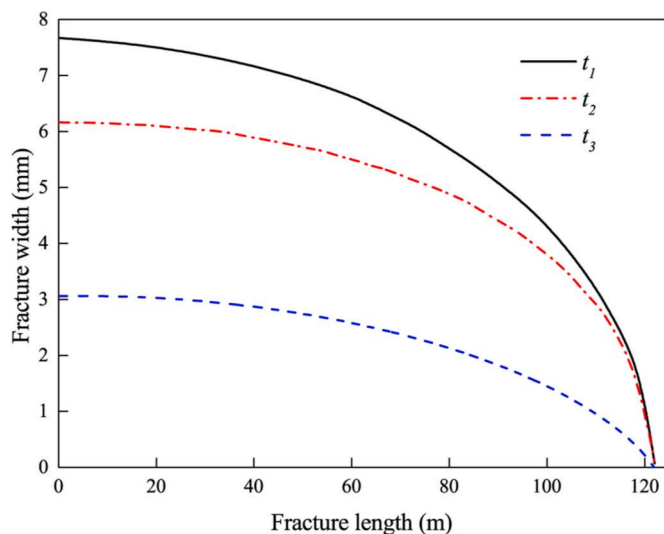


Fig. 8. Fracture opening at different time instants (t_1 , t_2 , and t_3) for cluster 1 of the Marcellus shale case.

hydraulic fracture can be seen from the curve shown in Fig. 7. Firstly, the width at the pumping point equals 7.66 mm at the end of the hydraulic fracturing stage (t_1). In the following shut-in period, as a direct result of the fluid leak-off into the surrounding formation (Taleghani et al., 2020), the fracture width gradually decreases. Afterwards, in the flow-back process of the fracturing fluid, the fracture width continues to decrease until the proppant pack takes effect to keep the fracture open at time instant t_3 , and the width at the pumping point drops by 60% to 3.06 mm. In other words, 40% of the fracture width is held by proppant grains. Then, as shown in Fig. 7, the width of the propped fracture will slowly decrease as a result of changes in effective stress and closure stress according to the relationship described in Eq. (26).

The history-matching result of the Marcellus shale case is presented in Fig. 9. A good match is found between the field data and the results of numerical simulation which simultaneously takes natural fractures, proppant distribution, geomechanics effects, proppant-related effects (deformation, embedment, and crushing), and gas diffusion and desorption into account. The gas flow rate without considering proppant-related effects and the gas flow rate without considering

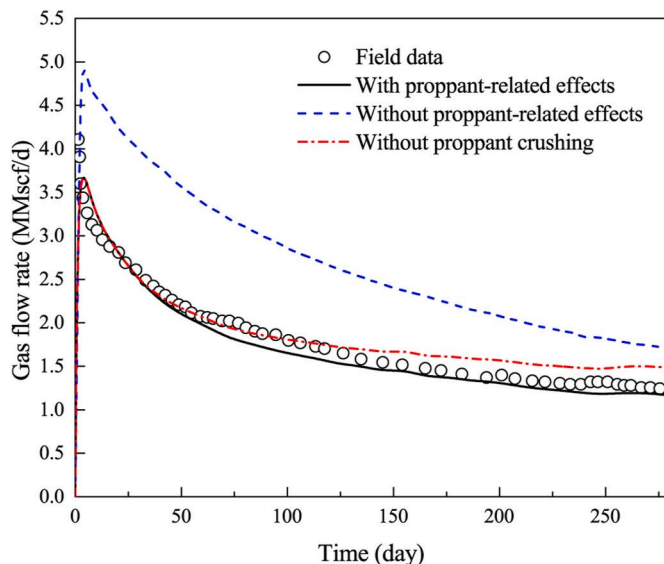


Fig. 9. History-matching result of the Marcellus shale case. Gas flow rates without considering proppant-related effects are also shown.

proppant crushing are also presented in Fig. 9. It can be clearly seen that the proppant-related effects play an important role in gas production, and the simulation without proppant-related effects will substantially overestimate the gas production. It can also be noticed that proppant crushing has no effect on the early stage gas production rate (Shi et al., 2018). However, with the increase of the closure stress, proppant crushing will dramatically decrease the conductivity of the propped fracture, leading to an overestimate of the gas production rate if proppant crushing effect has not been considered, as depicted in Fig. 9. The pressure distributions in the simulation model after 1 month, 9 months, and 5 years of production are shown in Fig. 10. During the first 1 month, the production is contributed primarily to the area near the surfaces of the hydraulic fracture. As production time increases, the active area increases, as shown in Fig. 10 (b). After 5 years of production, the most area that was penetrated by the hydraulic fracture has been well depleted; however, it can also be observed that the area in front of the hydraulic fracture still gives no contribution to the total production. The history-matching result of the Barnett shale case over a period of 4.5 years is shown in Fig. 11, from which good agreement can be seen. Consequently, the proposed model in this paper is capable of gas production simulation considering proppant behaviors such as deformation, embedment, and crushing based on the practical distribution of proppant obtained from the hydraulic fracturing simulation in which proppant transport is considered.

4. Results and discussion

When it comes to the evaluation and prediction of hydraulic fractured well performance, there is a large amount of literature (Cho et al., 2013; Javadpour, 2009; Wang, 2016; Wang and Marongiu-Porcu, 2015; Yu and Sepehrnoori, 2014; Yu et al., 2015) concerning the influence factors such as initial reservoir pressure, matrix permeability, fracture

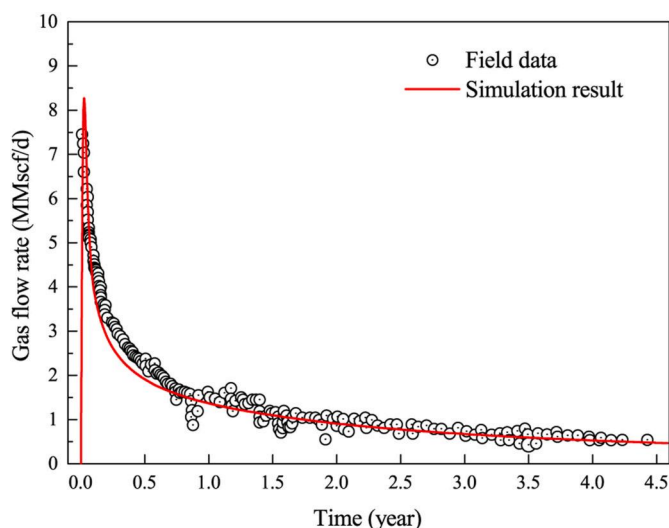


Fig. 11. History-matching results of the Barnett shale case.

network, geomechanics effects, non-Darcy flow, fracture spacing, gas desorption, and so on. However, the effects of proppant-related factors and creep of shale formation have been seldom reported in the literature. Hence, in the sensitivity studies, the uncertainty parameters are taken as the size of proppant, Young’s moduli and Poisson’s ratios of shale formation and proppant, proppant concentration, and viscosity coefficient of the formation. As listed in Table 2, all of the uncertainty parameters are chosen in wide ranges to cover more cases probably occur in practical applications.

4.1. Effects of proppant size

The mesh size (Economides and Martin, 2007) of proppant is one critical influence factor in the hydraulic fracturing treatment because the proppant size and its distribution directly influence the permeability of the proppant pack after its placement. Thus, proppant grains with typical diameters 0.1, 1.0, 1.5, and 2.0 mm have been studied in this paper, and all the other parameters are kept the same as the Marcellus shale case in Section 3. After the hydraulic fracturing simulation and the subsequent flowback and gas production simulation, the cumulative gas productions (CGP) over a period of 30 years are shown in Fig. 12, in which the result of the base case is also presented. For the sake of a clear presentation, the final cumulative gas productions (FCGP) at 30 years are also shown in the bottom right corner of Fig. 12. It can be found that the FCGP increases firstly, shows a maximum between 1.0 mm and 1.5 mm, and then decreases with the increase of D_p . It can also be observed that smaller proppant (0.1 mm) enables a slower decline of production rate in the long period compared with larger proppant (Liang et al., 2015). The decrease in FCGP is caused by two major reasons. Firstly, it is difficult for large proppant grains to be transported along with the slurry to the region around the fracture front due to the width limitation. In other words, the large proppant requires a larger fracture width to

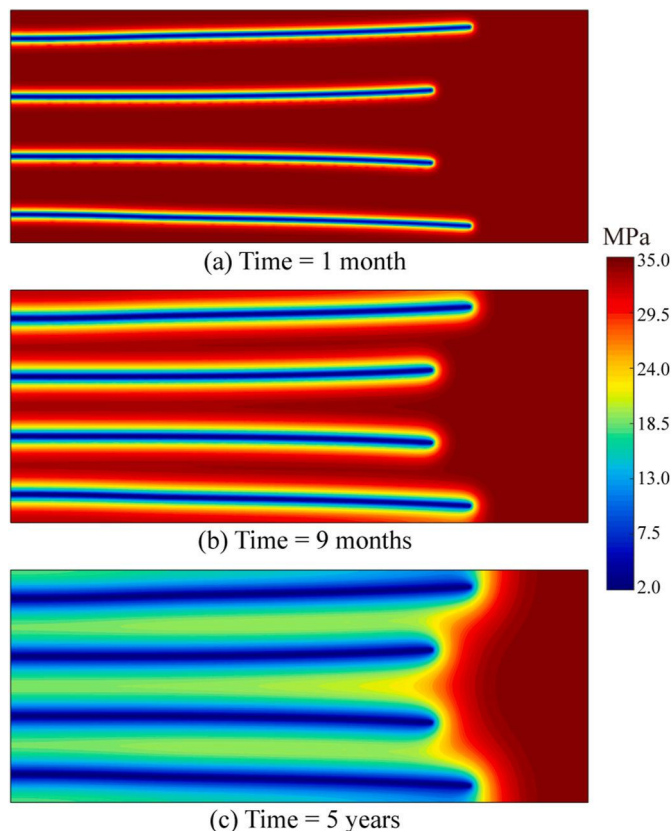


Fig. 10. Distributions of reservoir pressure at 1 month, 9 months, and 5 years of the Marcellus shale case.

Table 2

Parameters used in sensitivity studies.

Parameter	Base case	Minimum	Maximum	Unit
Proppant size, D_p		0.6	2.0	mm
Young’s modulus of proppant, E_p	20	5	80	GPa
Young’s modulus of formation, E_r	20	5	80	GPa
Poisson’s ratio of proppant, ν_p	0.2	0.1	0.3	–
Poisson’s ratio of formation, ν_r	0.2	0.1	0.3	–
Pumping concentration of proppant, c_{inj}	0.3	0.1	0.5	–
Viscosity coefficient of formation, η_r	0	0	1.0×10^{15}	Pa-s

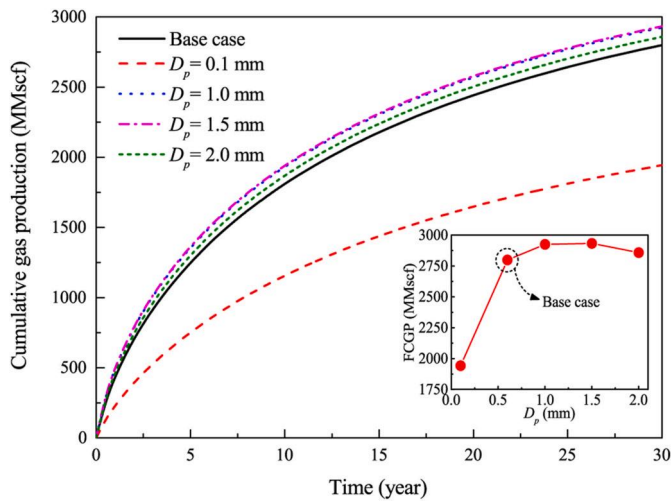


Fig. 12. Effects of proppant size on the cumulative gas production (CGP) in a 30-year period. The small graph shown in the bottom right corner gives the final cumulative gas production (FCGP) at 30 years.

enable transport without “bridging out” during the treatment (Economides and Martin, 2007). The second factor is the size effect of proppant grain on its strength, in other words, the increase of grain size reduces its tensile strength and proppant crushing is more likely to occur for the larger proppant.

In order to investigate to what extent the gas production is influenced by proppant crushing and size effect, we performed the simulations ignoring proppant crushing and the results are given in Fig. 13. The CGP monotonically increases as D_p increases (see the figure in the bottom right corner of Fig. 13), which is paradoxical to field observation results. For the base case, ignoring proppant crushing will overestimate the FCGP by 12%. Therefore, the proppant crushing and the size effect of proppant grains must be properly considered in the gas production simulation.

4.2. Effects of Young’s moduli of proppant and shale formation

The effects of E_p are given in Fig. 14 from which we can see that the CGP slightly increases for small E_p and stabilizes to a constant value with the increase of E_p . The FCGP increases by 4.6% from 2713.7 MMscf to 2838.8 MMscf when E_p increases from 5 GPa to 80 GPa. From the point

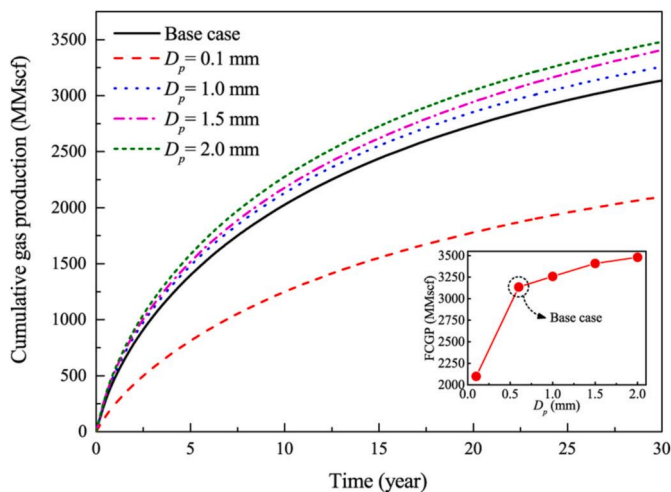


Fig. 13. Effects of proppant size on the CGP in a 30-year period without considering proppant crushing. The small graph shown in the bottom right corner gives the FCGP at 30 years.

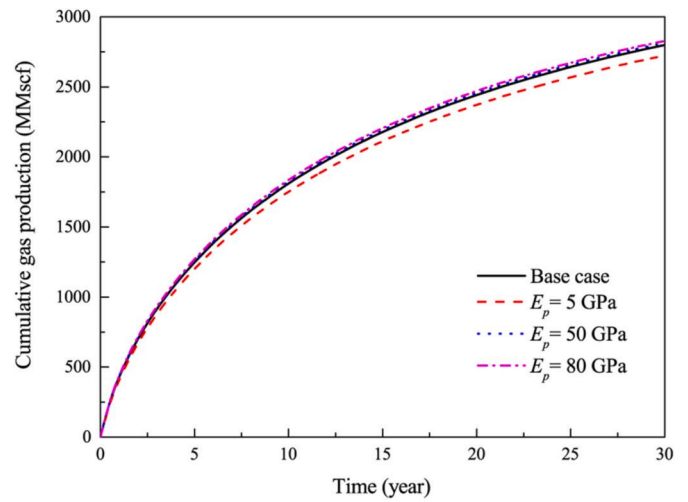


Fig. 14. Effects of E_p on the CGP in a 30-year period.

of view of mathematical model, the decreasing influence of E_p on the production is mainly due to the complex nonlinear relation between E_p and the fracture conductivity, which has been given in Eqs. (26) and (28). In addition, from the point of view of common sense, it is clear that the conductivity will not increase infinitely, but converges to a constant value, although the proppant has an infinitely large Young’s modulus.

The effects of E_r on the CGP are plotted in Fig. 15. The FCGP increases by 2.3% from 2761.4 MMscf to 2824.1 MMscf when E_r increases from 5 GPa to 80 GPa. Thus, it can be concluded that E_p has more pronounced effects than E_r .

4.3. Effects of Poisson’s ratios of proppant and shale formation

It can be seen from Eq. (26) that both ν_r and ν_p are necessary parameters for the calculation of propped fracture width when using the Hertzian contact theory. Accordingly, it is imperative to investigate the effects of Poisson’s ratios ranging from 0.1 to 0.3 on gas production. However, from the simulation results shown in Fig. 16 and Fig. 17 it can be observed that the Poisson’s ratios of both the proppant and the shale formation have negligible impacts on the CGP according to the proposed mathematical model. The reason is mainly due to the fact that the Poisson’s ratio is usually used in the form $1 - \nu^2$ in the numerical model (see Eq. (27)). This means that a large change in the Poisson’s ratio, say from 0.1 to 0.3 (by 200%), will only change $1 - \nu^2$ from 0.99 to 0.91 (by

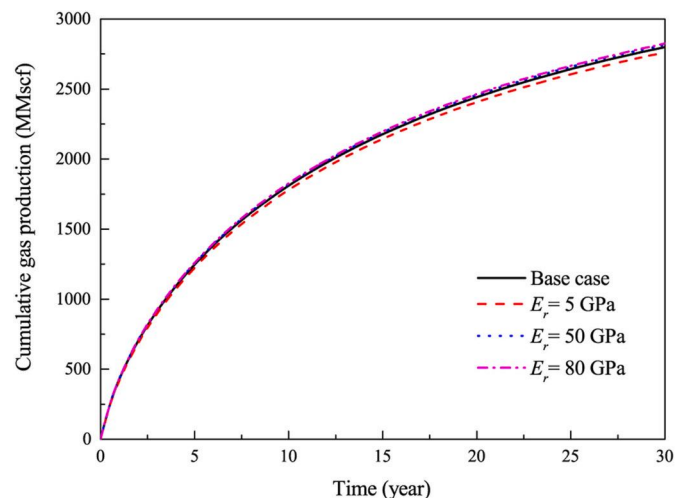


Fig. 15. Effects of E_r on the CGP in a 30-year period.

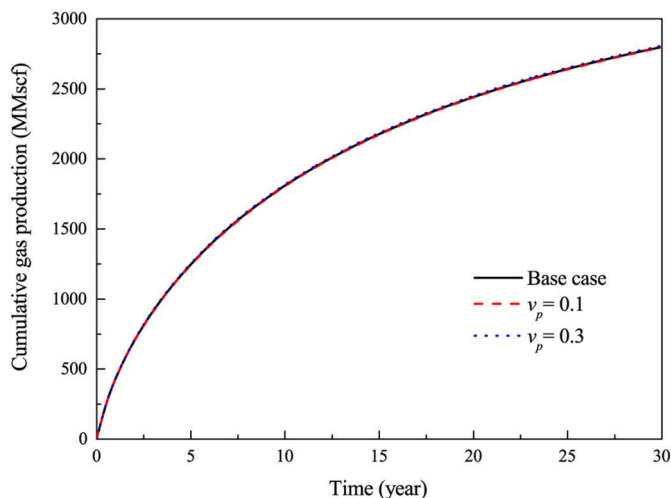


Fig. 16. Effects of ν_p on the CGP in a 30-year period.

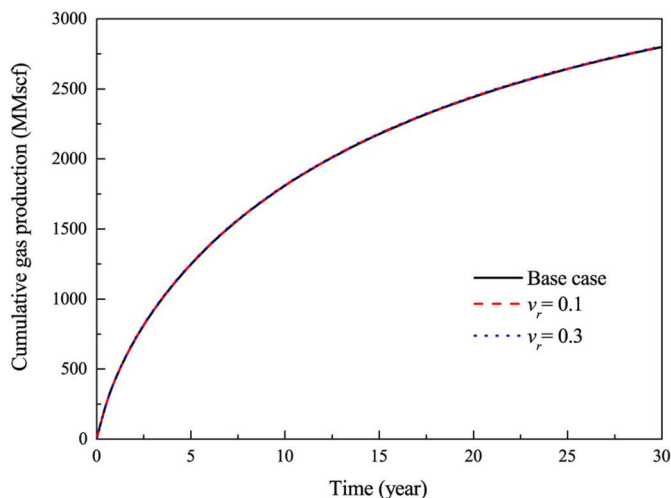


Fig. 17. Effects of ν_r on the CGP in a 30-year period.

8%). Therefore, the varying the Poisson's ratios have limited influence on the gas production.

4.4. Effects of proppant volumetric concentration

The amount of proppant pumped into the hydro-fracture is directly related to the volumetric concentration c_{inj} of proppant. The effects of c_{inj} on the CGP are illustrated in Fig. 18. As the concentration of injected proppant increases, the CGP increases (the FCGP increases significantly by 26.8% from 2316.5 MMscf to 2936.6 MMscf when c_{inj} increases from 0.1 to 0.5), which is consistent with a well-known conclusion (Wang and Chen, 2016) that higher proppant concentrations are more likely to result in a propped fracture with larger width and higher conductivity. However, as the concentration continues to increase, the CGP tends to a constant value, as shown in the small figure in the bottom right corner of Fig. 18. On the other hand, the completion cost also grows with increasing concentration. Put another way, the balance between production and cost should be taken into account when making decisions about proppant concentration.

4.5. Effects of shale formation creep

For the shale reservoir with high clay content, the effects of shale creep on the CGP are given in Fig. 19. It can be seen that time-dependent

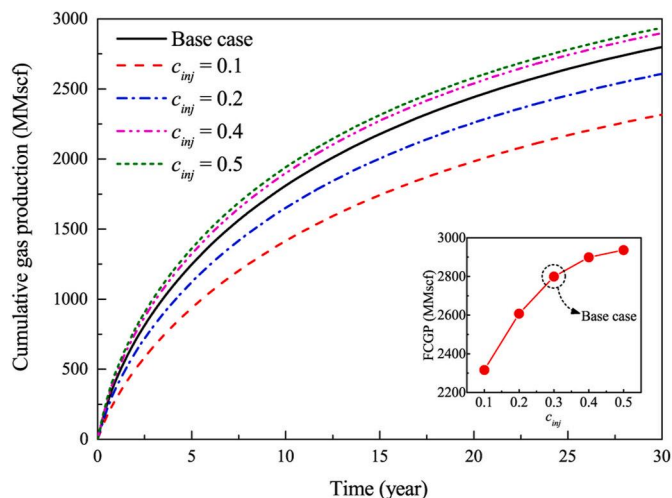


Fig. 18. Effects of proppant concentration on the CGP in a 30-year period. The small graph shown in the bottom right corner gives the FCGP at 30 years.

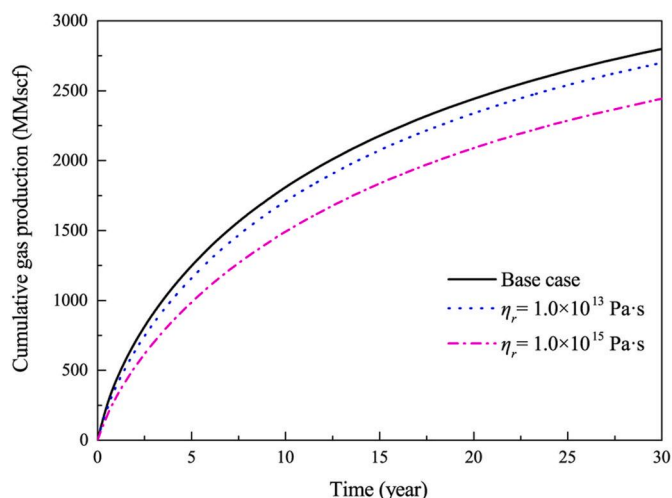


Fig. 19. Effects of viscosity coefficient of formation on the CGP in a 30-year period.

deformation of shale formation has a pronounced effect on gas production. The CGP decreases with increasing viscosity coefficient of formation, η_r . As η_r increases from zero to 1.0×10^{15} Pa s, the FCGP is dramatically reduced by 14.6% (from 2799.1 MMscf to 2442.1 MMscf). The decrease of the gas production is caused by two mechanisms: (1) The shale creep affects the width of the propped fracture and makes the fracture closes more rapidly by comparing to the elastic case, and (2) The shale creep affects the permeability of the reservoir.

As shown in Fig. 20, the effects of the uncertainty parameters listed in Table 2 on the CGP during a period of 30 years are summarized in a Tornado chart. According to the sensitivity studies based on the field data obtained from the Marcellus shale, it is found that proppant size has the highest impact on the CGP. The second influential parameter is proppant concentration, which is followed by viscosity of shale formation, and Young's modulus of proppant. Moreover, Young's modulus of formation is less influential, and Poisson's ratios have negligible influence compared to other parameters.

5. Conclusions

In this paper, an XFEM-based coupled method is proposed to perform hydraulic fracturing simulation to obtain the distribution of proppant

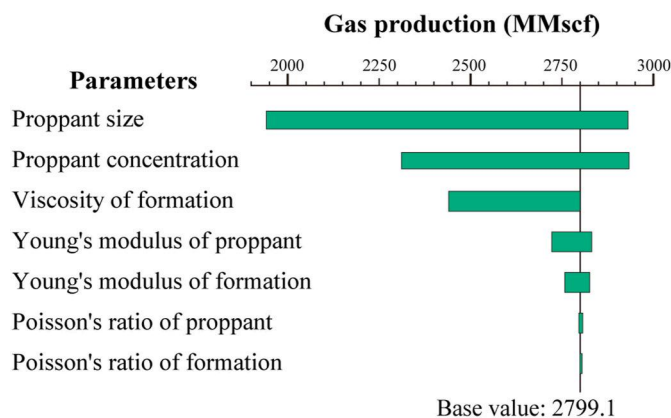


Fig. 20. Tornado chart of the sensitivity studies based on the data of Marcellus shale.

and the widths of the propped fracture, and then perform the flowback and gas production simulation to predict the cumulative gas production. The fracture closure during the shut-in and flowback process of fracturing fluid is considered. The reduction of the propped fracture conductivity caused by brittle failure, elastic deformation and embedment, size effects on the strength of proppant grains, creep behaviors of shale formation are considered when forecasting the gas production. Validations of history-matching of data collected from Marcellus shale and Barnett shale are performed to ensure the reliability of the proposed model. Then we carried out sensitivity studies on the effects of some key factors varied over wide ranges on the cumulative gas production based on the data of Marcellus shale. The numerical results obtained from this study indicate:

- (1) According to the sensitivity studies, it is found that proppant size has the most pronounced influence on the cumulative gas production, followed by proppant volumetric concentration, viscosity of shale formation, Young's modulus of proppant grains, and Young's modulus of shale formation. Furthermore, the effects of Poisson's ratios are negligible compared to other parameters.
- (2) As proppant size increases, the cumulative gas production increases and then reduces. The reduction in conductivity can be attributed to two factors. Firstly, the large proppant is hard to be brought to the region near the fracture tip due to the width limitation of the hydraulic fracture. Secondly, because of the size effect, proppant crushing is easier to occur for larger proppant.
- (3) It is demonstrated in this paper that the proppant crushing and the size effect of proppant grains must be properly considered in the gas production simulation. According to the sensitivity studies based on the data from Marcellus shale, it is found that ignoring proppant crushing will overestimate the final cumulative gas production by 12% at most.
- (4) For the shale reservoir with high clay content, time-dependent creep of shale formation has a profound effect on the cumulative gas production which decreases with increasing viscosity coefficient of the formation.
- (5) The cumulative gas production increases and then tends to a constant value as the concentration of injected proppant increases. Thus, some balance between production and cost must be sought when making decisions with regard to proppant concentration.

Credit author statement

Fang Shi: Conceptualization, Methodology, Software, Validation, Data curation, Writing, Visualization, Funding acquisition.

Declaration of competing interest

The authors declare that they have no known competing financial interests or personal relationships that could have appeared to influence the work reported in this paper.

Acknowledgements

This work was jointly supported by the National Natural Science Foundation of China [51904111], the Natural Science Foundation of Jiangsu Province [BK20170457], and the Open Fund for Jiangsu Key Laboratory of Advanced Manufacturing Technology [HGAMTL-1712].

Appendix A. Supplementary data

Supplementary data to this article can be found online at <https://doi.org/10.1016/j.petrol.2021.108523>.

References

- Adachi, J., Siebrits, E., Peirce, A., Desroches, J., 2007. Computer simulation of hydraulic fractures. *Int. J. Rock Mech. Min. Sci.* 44 (5), 739–757.
- Awoleke, O.O., Romero, J.D., Zhu, D., Hill, D., 2012. Experimental investigation of propped fracture conductivity in tight gas reservoirs using factorial design. In: SPE Hydraulic Fracturing Technology Conference. Society of Petroleum Engineers, The Woodlands, Texas, USA.
- Aybar, U., Eshkalak, M.O., Sepehrmoori, K., Patzek, T.W., 2014. The effect of natural fracture's closure on long-term gas production from unconventional resources. *J. Nat. Gas Sci. Eng.* 21, 1205–1213.
- Belytschko, T., Black, T., 1999. Elastic crack growth in finite elements with minimal remeshing. *Int. J. Numer. Methods Eng.* 45, 601–620.
- Cao, P., Liu, J., Leong, Y.-K., 2017. A multiscale-multiphase simulation model for the evaluation of shale gas recovery coupled the effect of water flowback. *Fuel* 199, 191–205.
- Chang, C., Zoback, M., 2009. Viscous creep in room-dried unconsolidated Gulf of Mexico shale (D): experimental results. *J. Petrol. Sci. Eng.* 69, 239–246.
- Cheng, L., Luo, Z., Yu, Y., Zhao, L., Zhou, C., 2019. Study on the interaction mechanism between hydraulic fracture and natural karst cave with the extended finite element method. *Eng. Fract. Mech.* 222, 106680.
- Cho, Y., Ozkan, E., Apaydin, O.G., 2013. Pressure-dependent natural-fracture permeability in shale and its effect on shale-gas well production. *SPE Reservoir Eval. Eng.* 16, 216–228.
- Chu, M.S., Chang, N.Y., 1980. Uniaxial creep of oil shale under elevated temperatures. In: *The 21st U.S. Symposium on Rock Mechanics (USRMS)*. American Rock Mechanics Association.
- Cipolla, C.L., Lolon, E., Mayerhofer, M.J., Warpinski, N.R., 2009. The effect of proppant distribution and un-propped fracture conductivity on well performance in unconventional gas reservoirs. In: SPE Hydraulic Fracturing Technology Conference. Society of Petroleum Engineers, The Woodlands, Texas.
- Clarkson, C.R., Williams-Kovacs, J.D., Qanbari, F., Behmanesh, H., Sureshjani, M.H., 2015. History-matching and forecasting tight/shale gas condensate wells using combined analytical, semi-analytical, and empirical methods. *J. Nat. Gas Sci. Eng.* 26, 1620–1647.
- Crouch, S.L., Starfield, A.M., 1990. *Boundary Element Methods in Solid Mechanics*. Unwin & Hyman, London.
- Cui, G., et al., 2020. Multidomain two-phase flow model to study the impacts of hydraulic fracturing on shale gas production. *Energy Fuel* 34 (4), 4273–4288.
- Dahi-Taleghani, A., Olson, J.E., 2011. Numerical modeling of multistranded-hydraulic-fracture propagation: accounting for the interaction between induced and natural fractures. *SPE J.* 16 (3), 575–581.
- Dontsov, E.V., Peirce, A.P., 2015. Proppant transport in hydraulic fracturing: crack tip screen-out in KGD and P3D models. *Int. J. Solid Struct.* 63, 206–218.
- Economides, M.J., Martin, T., 2007. *Modern Fracturing Enhancing Natural Gas Production*. BJ Services Company, Houston, TX.
- Erdogan, F., Sih, G.C., 1963. On the crack extension in plates under plane loading and transverse shear. *J. Basic. Eng-T. ASME* 85 (4), 519–525.
- Florence, F.A., Rushing, J., Newsham, K.E., Blasingame, T.A., 2007. Improved permeability prediction relations for low permeability sands. In: *Rocky Mountain Oil & Gas Technology Symposium*. Society of Petroleum Engineers, Denver, Colorado, U.S.A.
- Fredd, C.N., McConnell, S.B., Boney, C.L., England, K.W., 2001. Experimental study of fracture conductivity for water-fracturing and conventional fracturing applications. *SPE J.* 6 (3), 288–298.
- Gambarotta, L., Lagomarsino, S., 1993. A microcrack damage model for brittle materials. *Int. J. Solid Struct.* 30, 177–198.
- Gordeliy, E., Peirce, A., 2013a. Coupling schemes for modeling hydraulic fracture propagation using the XFEM. *Comput. Methods Appl. Math.* 253, 305–322.
- Gordeliy, E., Peirce, A., 2013b. Implicit level set schemes for modeling hydraulic fractures using the XFEM. *Comput. Methods Appl. Math.* 266, 125–143.

- Grieser, W.V., Shelley, R.F., Soliman, M.Y., 2009. Predicting production outcome from multi-stage, horizontal Barnett completions. In: SPE Production and Operations Symposium, Oklahoma City, Oklahoma.
- Hammond, P.S., 1995. Settling and slumping in a Newtonian slurry, and implications for proppant placement during hydraulic fracturing of gas wells. *Chem. Eng. Sci.* 50 (20), 3247–3260.
- Han, J., Wang, J.Y., Puri, V., 2016a. A fully coupled geomechanics and fluid flow model for proppant pack failure and fracture conductivity damage analysis. *J. Nat. Gas Sci. Eng.* 31, 546–554.
- Han, J., et al., 2016b. Numerical Study of Proppant Transport in Complex Fracture Geometry, SPE Low Perm Symposium. Society of Petroleum Engineers, Denver, Colorado, USA.
- Huang, J., Ghassemi, A., 2013. Simulating geomechanical evolution of fractured shale reservoir using a poro-viscoelastic constitutive model. In: 47th U.S. Rock Mechanics/Geomechanics Symposium. American Rock Mechanics Association, San Francisco, California.
- Huang, J., Xu, S., Yi, H., Hu, S., 2014. Size effect on the compression breakage strengths of glass particles. *Powder Technol.* 268, 86–94.
- Javadpour, F., 2009. Nanopores and apparent permeability of gas flow in mudrocks (shales and siltstone). *J. Can. Pet. Technol.* 48, 16–21.
- Jiang, J., Younis, R.M., 2015. Numerical study of complex fracture geometries for unconventional gas reservoirs using a discrete fracture-matrix model. *J. Nat. Gas Sci. Eng.* 26, 1174–1186.
- Johnson, K.L., 1985. Contact Mechanics. Cambridge University Press, Cambridge.
- Johnson, K.L., O'Connor, J.J., Woodward, A.C., 1973. The effect of the indenter elasticity on the Hertzian fracture of brittle materials. *Proc. Roy. Soc. Lond.* 334, 95–117.
- Khoei, A.R., 2014. Extended Finite Element Method: Theory and Applications. John Wiley & Sons, London.
- Khoei, A.R., Hirmand, M., Vahab, M., Bazargan, M., 2015. An enriched FEM technique for modeling hydraulically driven cohesive fracture propagation in impermeable media with frictional natural faults: numerical and experimental investigations. *Int. J. Numer. Methods Eng.* 104 (6), 439–468.
- Khoei, A.R., Vahab, M., Hirmand, M., 2016. Modeling the interaction between fluid-driven fracture and natural fault using an enriched-FEM technique. *Int. J. Fract.* 197, 1–24.
- Klinkenberg, L.J., 1941. The Permeability of Porous Media to Liquids and Gases, Drilling and Production Practice. American Petroleum Institute, New York.
- Kong, B., Fathi, E., Ameri, S., 2015. Coupled 3-D numerical simulation of proppant distribution and hydraulic fracturing performance optimization in Marcellus shale reservoirs. *Int. J. Coal Geol.* 147–148, 35–45.
- Lacy, L.L., Rickards, A.R., Ali, S.A., 1997. Embedment and fracture conductivity in soft formations associated with HEC, borate and water-based fracture designs. In: SPE Annual Technical Conference and Exhibition. Society of Petroleum Engineers, San Antonio, Texas, USA.
- Langmuir, I., 1918. The adsorption of gases on plane surfaces of glass, mica and platinum. *J. Am. Chem. Soc.* 40, 1361–1403.
- Lecampion, B., 2009. An extended finite element method for hydraulic fracture problems. *Commun. Numer. Methods Eng.* 25 (2), 121–133.
- Li, H., Wang, K., Xie, J., Li, Y., Zhu, S., 2016. A new mathematical model to calculate sand-packed fracture conductivity. *J. Nat. Gas Sci. Eng.* 35, 567–582.
- Li, K., Gao, Y., Lyu, Y., Wang, M., 2015. New mathematical models for calculating proppant embedment and fracture conductivity. *SPE J.* 20 (3), 496–507.
- Li, Y., Ghassemi, A., 2012. Creep Behavior of Barnett, Haynesville, and Marcellus Shale, 46th U.S. Rock Mechanics/Geomechanics Symposium. American Rock Mechanics Association, Chicago, Illinois.
- Liang, F., Sayed, M., Al-Muntasheri, G., Chang, F.F., 2015. Overview of existing proppant technologies and challenge. In: SPE Middle East Oil & Gas Show and Conference. Society of Petroleum Engineers, Manama, Bahrain.
- Liu, C., et al., 2019. Production analysis in shale gas reservoirs based on fracturing enhanced permeability areas. *Sci. China Phys. Mech. Astron.* 62, 104611.
- Liu, J., et al., 2016a. Flow consistency between non-Darcy flow in fracture network and nonlinear diffusion in matrix to gas production rate in fractured shale gas reservoirs. *Transport Porous Media* 111, 97–121.
- Liu, P., et al., 2016b. Multi-phase fracturing fluid leakoff model for fractured reservoir using extended finite element method. *J. Nat. Gas Sci. Eng.* 28, 548–557.
- Ma, T., Rutqvist, J., Oldenburg, C.M., Liu, W., Chen, J., 2017. Fully coupled two-phase flow and poromechanics modeling of coalbed methane recovery: impact of geomechanics on production rate. *J. Nat. Gas Sci. Eng.* 45, 474–486.
- Marques, S.P.C., Creus, G.J., 2012. Computational Viscoelasticity. Springer, Berlin.
- Mayerhofer, M.J., Lonon, E.P., Youngblood, J.E., Heinze, J.R., 2006. Integration of Microseismic-Fracture-Mapping Results with Numerical Fracture Network Production Modeling in the Barnett Shale. SPE Annual Technical Conference and Exhibition, San Antonio, Texas, USA.
- Moës, N., Dolbow, J., Belytschko, T., 1999. A finite element method for crack growth without remeshing. *Int. J. Numer. Methods Eng.* 46 (1), 131–150.
- Mohammadnejad, T., Khoei, A.R., 2013. An extended finite element method for hydraulic fracture propagation in deformable porous media with the cohesive crack model. *Finite Elem. Anal. Des.* 73, 77–95.
- Neto, L.B., Khanna, A., Kotousov, A., 2015. Conductivity and performance of hydraulic fractures partially filled with compressible proppant packs. *Int. J. Rock Mech. Min. Sci.* 74, 1–9.
- Osholake, T., Wang, J.Y., Ertekin, T., 2013. Factors affecting hydraulically fractured well performance in the Marcellus shale gas reservoirs. *J. Energy Resour. Technol.* 135 (1), 013402.
- Ouwerkerk, C.E.D., 1991. A micro-mechanical connection between the single-particle strength and the bulk strength of random packings of spherical particles. *Powder Technol.* 65, 125–138.
- Ouyang, S., Carey, C.F., Yew, C.H., 1997. An adaptive finite element scheme for hydraulic fracturing with proppant transport. *Int. J. Numer. Methods Fluid.* 24 (7), 645–670.
- Pan, Z., Connell, L.D., 2015. Reservoir simulation of free and adsorbed gas production from shale. *J. Nat. Gas Sci. Eng.* 22, 359–370.
- Press, W.H., Teukolsky, S.A., Vetterling, W.T., Flannery, B.P., 1992. Numerical Recipes in Fortran: the Art of Scientific Computing. Cambridge University Press, New York.
- Seales, M.B., Dillmore, R., Ertekin, T., Wang, J.Y., 2016. A Numerical Study of Factors Affecting Fracture-Fluid Cleanup and Produced Gas/water in Marcellus Shale: Part II. SPE J., Preprint.
- Shi, F., Wang, X., Liu, C., Liu, H., Wu, H., 2016. A coupled extended finite element approach for modeling hydraulic fracturing in consideration of proppant. *J. Nat. Gas Sci. Eng.* 33, 885–897.
- Shi, F., Wang, X., Liu, C., Liu, H., Wu, H., 2017. An XFEM-based method with reduction technique for modeling hydraulic fracture propagation in formations containing frictional natural fractures. *Eng. Fract. Mech.* 173, 64–90.
- Shi, F., Wang, X., Liu, C., Liu, H., Wu, H., 2018. An XFEM-based numerical model to calculate conductivity of propped fracture considering proppant transport, embedment and crushing. *J. Petrol. Sci. Eng.* 167, 615–626.
- Shiozawa, S., McClure, M., 2016. Simulation of proppant transport with gravitational settling and fracture closure in a three-dimensional hydraulic fracturing simulator. *J. Petrol. Sci. Eng.* 138, 298–314.
- Sokolinsky, V.S., Indermuehle, K.C., Hurtado, J.A., 2011. Numerical simulation of the crushing process of a corrugated composite plate. *Composites Part A* 42, 1119–1126.
- Sone, H., Zoback, M.D., 2014. Time-dependent deformation of shale gas reservoir rocks and its long-term effect on the in situ state of stress. *Int. J. Rock Mech. Min. Sci.* 69, 120–132.
- Steinhaus, H., 1999. Mathematical Snapshots. Dover Publications, New York.
- Taleghani, A.D., Cai, Y., Pouya, A., 2020. Fracture closure modes during flowback from hydraulic fractures. *Int. J. Numer. Anal. Methods GeoMech.* 44 (12), 1695–1704.
- Taleghani, A.D., Olson, J.E., 2014. How natural fractures could affect hydraulic-fracture geometry. *SPE J.* 19 (1), 161–171.
- Tomac, I., Gutierrez, M., 2013. Numerical Study of Horizontal Proppant Flow and Transport in a Narrow Hydraulic Fracture 47th U.S. Rock Mechanics/Geomechanics Symposium. American Rock Mechanics Association, San Francisco, California.
- Tsoungis, O., Vallet, D., Charmet, J.-C., Roux, S., 1999. Size effects in single grain fragmentation. *Granul. Matter* 2, 19–27.
- Wang, H., 2016. What factors control shale-gas production and production-decline trend in fractured systems: a comprehensive analysis and investigation. SPE J. Preprint (Preprint): Preprint.
- Wang, H., Marongiu-Porcu, M., 2015. Impact of shale-gas apparent permeability on production: combined effects of non-Darcy flow/gas-slippage, desorption, and geomechanics. *SPE Reservoir Eval.* 18, 495–507.
- Wang, S., Chen, S., 2016. Evaluation and prediction of hydraulic fractured well performance in montney formations using a data-driven approach. In: SPE Western Regional Meeting. Society of Petroleum Engineers, Anchorage, Alaska, USA.
- Warpinski, N.R., 1989. Elastic and viscoelastic calculations of stresses in sedimentary basins. *SPE Form. Eval.* 4 (4), 522–530.
- Wei, S., Jin, Y., Xia, Y., Lin, B., 2020. The flowback and production analysis in sub-saturated fractured shale reservoirs. *J. Petrol. Sci. Eng.* 186, 106694.
- Weng, X., Kresse, O., Cohen, C.-E., Wu, R., Gu, H., 2011. Modeling of hydraulic-fracture-network propagation in a naturally fractured formation. *SPE Prod. Oper.* 26 (4), 368–380.
- Yan, X., Huang, Z., Zhang, Q., Fan, D., Yao, J., 2020. Numerical investigation of the effect of partially propped fracture closure on gas production in fractured shale reservoirs. *Energies* 13, 5339.
- Yeager, B.B., Meyer, B.R., 2010. Injection/fall-off testing in the marcellus shale: using reservoir knowledge to improve operational efficiency. In: SPE Eastern Regional Meeting. Society of Petroleum Engineers, Morgantown, West Virginia, USA.
- Yu, W., Sepehrmoori, K., 2013. Simulation of proppant distribution effect on well performance in shale gas reservoirs. In: SPE Unconventional Resources Conference Canada. Society of Petroleum Engineers, Calgary, Alberta, Canada.
- Yu, W., Sepehrmoori, K., 2014. Simulation of gas desorption and geomechanics effects for unconventional gas reservoirs. *Fuel* 116, 455–464.
- Yu, W., Zhang, T., Du, S., Sepehrmoori, K., 2015. Numerical study of the effect of uneven proppant distribution between multiple fractures on shale gas well performance. *Fuel* 142, 189–198.
- Zhang, J., 2014. Theoretical conductivity analysis of surface modification agent treated proppant. *Fuel* 134, 166–170.
- Zhang, J., Wong, T.-F., Davis, D.M., 1990. Micromechanics of pressure-induced grain crushing in porous rocks. *J. Geophys. Res.* 95, 341–352.
- Zhang, T., et al., 2017. Numerical investigation of the well shut-in and fracture uncertainty on fluid-loss and production performance in gas-shale reservoirs. *J. Nat. Gas Sci. Eng.* 46, 421–435.
- Zhou, L., Houa, M.Z., Goua, Y., Lia, M., 2014. Numerical investigation of a low-efficient hydraulic fracturing operation in a tight gas reservoir in the North German Basin. *J. Petrol. Sci. Eng.* 120, 119–129.